Generating high fidelity wind fields from the wind speed correlation tensor

Matteo Faccioni [1, 2], Daniel Kiehn[3], and Patrick Vrancken[1]

[1]Deutsches Zentrum für Luft- und Raumfahrt (DLR), Institut für Physik der Atmosphäre, Oberpfaffenhofen, Germany
[2]Technical University of Munich, School of Engineering and Design, Department of Aerospace and Geodesy, Institute of Astronomical and Physical Geodesy, Munich, Germany
[3]DLR Institute of Flight Systems, Braunschweig, Germany

Correspondence: Matteo Faccioni (matteo.faccioni@dlr.de)

Abstract. In this publication a new method to generate stochastic representations of homogeneous and isotropic wind fields is presented. In contrast to the typically employed algorithm, the new approach is based on the wind speed correlation tensor. This allows simulating a homogeneous and isotropic turbulent wind field with very high accuracy, achieving a deviation of the obtained dataset's structure function from the theoretical one of at least one order of magnitude lower than the commonly used method. A compensation method to decrease this error even further is proposed. Moreover, being a generic method, it can be used to simulate other Gaussian phenomena (e.g., temperature or index of refraction fluctuations) on various spatial domains with uniformly spaced rectangular grid shapes. The motivation for this paper is to develop an algorithm able to synthesize high fidelity homogeneous and isotropic wind speed datasets within an arbitrary model domain geometry without the need for optimizing weighting parameters. This is achieved by eliminating the band-pass effect of the discrete Fourier transform inherent to the typically used algorithm.

1 Introduction

In recent decades, researchers and engineers have increasingly relied on the use of synthetic datasets to represent complex physical phenomena during the design process. Examples include the generation of wind speed along the three spatial dimensions, used in the design of airframe structures (cf. Hoblit (1988) or the aviation regulations CS25 (2023)) and the computation of wind turbine loads (as specified in IEC61400-1 (2019)). Further, synthetic datasets are relevant for the generation of phase screens, used in the modeling of optical propagation through the turbulent atmosphere (Andrews and Phillips, 2005). For this reason, within the last sixty years, several stochastic synthesis methods have been developed, in particular for phenomena that are considered Gaussian and stationary (e.g., temperature fluctuations and homogeneous, isotropic turbulence). These methods are based on different statistical approaches, including modal decomposition techniques (Fried, 1965), autoregressive models (Baran and Infield, 1995), linear dynamical system solutions (Beghi et al., 2011), machine learning (Wold et al., 2024), or the spectral representation of the phenomenon. This last family of algorithms can be further divided into the methods computing the dataset by means of the relation between the phenomenon's correlation function and power spectral density (PSD) (Borgman et al., 1984), the ones embedding the correlation matrix, computed from the correlation function, in a circulant matrix, and

generating the dataset from its eigenvalues decomposition (Dietrich and Newsam, 1993; Wood and Chan, 1994), and the ones synthesizing the dataset directly from the spectrum of the phenomenon (Mann, 1998). The latter class of algorithms, referred to in this article as *random phase method* (RPM) after Wilson (1998), has been very widely used in the realization of stochastic wind fields in the last twenty years (Friedrich et al., 2022; Chen et al., 2022). However, to the authors' knowledge, there is still no algorithm capable of synthesizing a high-fidelity wind field dataset (i.e., achieving a deviation from the theoretical correlation of less than 1%) on different spatial domains (e.g., a cuboid of $2000\,\mathrm{m} \times 2000\,\mathrm{m} \times 2000\,\mathrm{m}$ and a parallelepiped of $8000\,\mathrm{m} \times 500\,\mathrm{m} \times 500\,\mathrm{m}$) without the need for specific optimization or weighting parameters. The here proposed method builds on the RPM and the Fourier integral method (FIM) developed by Pardo-Iguzquiza and Chica-Olmo (1993), and solves the optimization issues needed for different spatial domains, allowing one to obtain a high fidelity 1-D, 2-D, or 3-D dataset on a wide range of uniformly spaced spatial domains with rectangular grid shapes. This is achieved using the relation between the correlation function and the PSD, eliminating the band-pass effect of the discrete Fourier transform (DFT) arising while using the RPM. Since this method is based on the correlation tensor, it has been decided to call it the *correlation-based random phase method* (CB-RPM). The paper is structured as follows: in the first section, the theory behind the RPM is presented. The dataset's verification procedure is described in the second section, while the RPM's discretization errors are explained using an example in the third section. In the fourth section the theory behind CB-RPM is presented, while in the fifth section the error of the latter method is computed for different wind fields at different spatial domains. Finally, in the sixth section, the RPM and the CB-RPM results are compared for different spatial domains.

2 The legacy approach: RPM

First applied by Shinozuka and Jan (1972) in the field of structural analysis, the approach to use the PSD in the synthesis of stochastic datasets has become basically *the* method of choice in different areas, such as wind engineering (Mann, 1998), acoustics (Wilson, 1998), and astronomy (Lane et al., 1992). Considering a homogeneous random field $\boldsymbol{u}(\boldsymbol{s})$, where $\boldsymbol{s}$ is the space vector and $\boldsymbol{u}$ is a vector composed of the components along the three axes $\boldsymbol{u}(\boldsymbol{s}) = (u_x(\boldsymbol{s}), u_y(\boldsymbol{s}), u_z(\boldsymbol{s}))$, the field's spectral representation can be written in the form of a Fourier-Stieltjes integral with a random complex amplitude $d\boldsymbol{\psi}(\boldsymbol{k})$ (Cramer and Leadbetter, 1967):

$$\boldsymbol{u}(\boldsymbol{s}) = \int_{-\infty}^{+\infty} e^{\mathrm{i}\boldsymbol{k}\boldsymbol{s}} d\boldsymbol{\psi}(\boldsymbol{k})\,; \tag{1}$$

where $\boldsymbol{k}$ is the wavenumber vector, and i is the imaginary unit. The process $\boldsymbol{\psi}(\boldsymbol{k})$ is directly related with the PSD $\Phi(\boldsymbol{k})$ by (Cramer and Leadbetter, 1967):

$$\overline{|d\boldsymbol{\psi}(\boldsymbol{k})^2|} = \Phi(\boldsymbol{k}) d\boldsymbol{k}\,; \tag{2}$$

where the overline symbol $\overline{\psi}$ denotes the mean. In the case of a three-dimensional turbulent wind field, the PSD is described by the 3×3 tensor $\Phi_{pq}(\boldsymbol{k})$ (Batchelor, 1953), where the subscripts p and q are the tensor indices. Considering a discretized

volume, the integral in Eq. (1) can be approximated with a discrete Fourier series (Mann, 1998):

$$u_p(\boldsymbol{s}) = \sum_{j=1}^{N} e^{\mathrm{i}k_j \boldsymbol{s}} C_{pq}(\boldsymbol{k}) \mu_q(\boldsymbol{k}) \,; \tag{3}$$

where N is the number of points in the dataset (i.e., the total number of the grid's pixels), $\mu_q(\boldsymbol{k})$ is a set of complex random variables with zero mean and unit variance, and $C_{pq}(\boldsymbol{k})$ are the Fourier coefficients, related with the wind speed tensor by (Mann, 1998):

$$C^*_{pt} C_{qt} = \frac{(2\pi)^m}{V} \Phi_{pq}(\boldsymbol{k}) \,; \tag{4}$$

where V is the volume of the grid considered, the star symbol * denotes the complex conjugate, and m is the number of dimensions of the considered spatial domain (e.g., $m = 2$ for a 2-D grid). Once computed the Fourier coefficients C_{pq}, Eq. (3) can be solved efficiently using the inverse Fourier transform (Cooley and Tukey, 1965):

$$u_p(\boldsymbol{s}) = \mathrm{Re}/\mathrm{Im} \left\{ \mathcal{F}^{-1} \left(\mu(\boldsymbol{k}) \frac{(2\pi)^{m/2}}{\sqrt{V}} N \sqrt{\Phi_{pq}(\boldsymbol{k})} \right) \right\} ; \tag{5}$$

where Re/Im means that either the real or imaginary component of the result can be used, and $\mathcal{F}^{-1}$ stands for the Discrete Inverse Fourier Transform (DIFT). The $\sqrt{\Phi_{pq}(\boldsymbol{k})}$ term is computed using matrix decomposition techniques, such as the Cholesky (1910) decomposition, or the dimension-dependent factorizations suggested in Mann (1998). The result is not unique, differing accordingly to the implemented technique, and it can be numerically challenging to compute.

3 Verification of the synthesized dataset

To check the quality of the dataset generated using Eq. (5) (i.e., computing the dataset's correlation deviation from the theoretical one), the dataset's structure function, D, can be compared with the theoretical one, D_{th}, as suggested by Johansson and Gavel (1994). D can be computed in two different ways:

- directly from its definition (Tatarski, 1961):

  $$D(\boldsymbol{r}) = \overline{\left(u_x(\boldsymbol{s}+\boldsymbol{r}) - u_x(\boldsymbol{s})\right)^2} ; \tag{6}$$

  where $\boldsymbol{r}$ is the separation vector, defined as the radial distance from the center of the grid;

- or, in a faster way, by means of the relation between the structure function and the correlation function, B, a statistical function that describes the mutual relation between the fluctuations of a physical phenomenon at different spatial positions. The procedure is the following:

  1. Compute the dataset's PSD, $\Phi(\boldsymbol{k})$, as:

     $$\Phi(\boldsymbol{k}) = \overline{|\mathcal{F}(u(\boldsymbol{s}))^2|} = \frac{\mathcal{F}(u(\boldsymbol{s}))\mathcal{F}(u(\boldsymbol{s}))^*}{N} ; \tag{7}$$

     where the symbol $\mathcal{F}$ denotes the DFT.

2. Compute the dataset's correlation function $B(\boldsymbol{r})$. According to the Wiener–Khinchin theorem (Wiener, 1930), $B(\boldsymbol{r})$ is the inverse Fourier transform of $\Phi(\boldsymbol{k})$;

$$B(\boldsymbol{r}) = \mathcal{F}^{-1}(\Phi(\boldsymbol{k}))\,. \tag{8}$$

3. Finally, the dataset's structure function can be computed as:

$$D(\boldsymbol{r}) = 2(B(\boldsymbol{0}) - B(\boldsymbol{r}))\,; \tag{9}$$

where $\boldsymbol{0}$ is the null vector.

Once the dataset's structure function is computed using Eq. (9), the dataset's error can be quantified as:

$$\varepsilon(\boldsymbol{r}) = \left| \frac{D(\boldsymbol{r})}{D_{th}(\boldsymbol{r})} - 1 \right|. \tag{10}$$

For a more detailed explanation of the structure function and the correlation function, the interested reader is referred to Tatarski (1961).

4 RPM's discretization errors

As an example of the RPM application, consider generating a 2-D wind field representing only the velocity component along the x-axis, $u_x(\boldsymbol{s})$. In this case, Eq. (4) becomes:

$$C_{xx}(\boldsymbol{k}) = \sqrt{\Phi_{xx}(\boldsymbol{k})}\,; \tag{11}$$

consequently, $u_x(\boldsymbol{s})$ is:

$$u_x(\boldsymbol{s}) = \mathrm{Re/Im}\left\{ \mathcal{F}^{-1}\left(\mu(\boldsymbol{k}) \frac{2\pi}{L_x L_y} N_x N_y \sqrt{\Phi_{xx}(\boldsymbol{k})} \right) \right\}; \tag{12}$$

where L_i is the domain size along the i-th direction, N_i is the number of pixels along the i-th direction, and $\mu(\boldsymbol{k})$ is a $N_x \times N_y$ matrix of complex random variables with zero mean and unit variance. To test the RPM accuracy, a single wind field has been generated using Eq. (12) considering a von Kármán (VK) spectrum with a turbulence outer scale of $L_0 = 756\ \mathrm{m}$, on a square grid of dimensions $3L_0 \times 3L_0$. The expected dataset' structure function is computed by setting $\mu(\boldsymbol{k}) = \boldsymbol{1}$ in Eq. (12). The theoretical structure function is computed using Eq. (9), where in the case of the velocity component along the x-axis in a 2-D domain the correlation function $B(\boldsymbol{r})$ is (Batchelor, 1953):

$$B(\boldsymbol{r}) = \sigma^2 \left[\frac{r_x^2}{\boldsymbol{r}^2} f(\boldsymbol{r}) + \frac{r_y^2}{\boldsymbol{r}^2} g(\boldsymbol{r}) \right]; \tag{13}$$

where σ^2 is the wind speed variance, and $f(\boldsymbol{r})$ and $g(\boldsymbol{r})$ are the longitudinal and lateral correlation functions respectively. Assuming a VK spectrum, these can be expressed as (Wilson, 1998):

$$f(\boldsymbol{r}) = \frac{2}{\Gamma(1/3)} \left(\frac{\boldsymbol{r}}{2L_0} \right)^{1/3} K_{1/3}\left(\frac{\boldsymbol{r}}{L_0} \right); \tag{14}$$

$$g(\boldsymbol{r}) = \frac{2}{\Gamma(1/3)} \left(\frac{\boldsymbol{r}}{2L_0} \right)^{1/3} \left[K_{1/3}\left(\frac{\boldsymbol{r}}{L_0} \right) - \frac{\boldsymbol{r}}{2L_0} K_{2/3}\left(\frac{\boldsymbol{r}}{L_0} \right) \right]; \tag{15}$$

where K_ν is the modified Bessel function of the second kind of order ν. The generated wind field, its structure function, and the expected one, computed substituting Eq. (13) in Eq. (9), are represented in Fig. (1). By analyzing the expected and theoretical

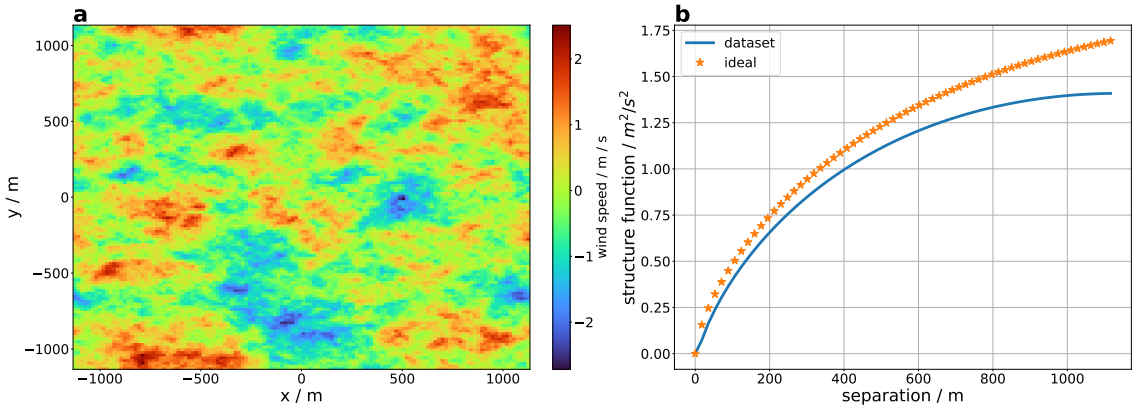

Figure 1. A 2-D wind field example generated by the RPM. Fig1a: a single wind field generated using the RPM. Fig1b: theoretical structure function in orange stars, dataset's expected structure function in blue.

structure functions, it is clear that the generated wind field does not properly represent the required statistics, underestimating the spectral power, and thus the wind speed variance, especially for larger values of the separation vector $\boldsymbol{r}$.

This error arises due to the fact that the PSD is not a bandwidth-limited function in the desired wavenumber domain, hence the implementation of the DFT generates a sampling error, as stated by the Nyquist-Shannon sampling theorem (Shannon, 1949). In fact, by using the DFT, the wavenumber domain on which the PSD is computed is determined by the grid's spatial resolution, as represented in Fig. (2), where it is clear how the spatial grid acts as a sort of band-pass filter, considering only part of the spectra. A possible way to circumvent the low wavenumbers' power underestimation is to increase the actual spatial grid size while maintaining the same spatial resolution in order to consider the lower wavenumbers. However, this approach depends on the considered PSD and on the grid shape, so it has to be optimized for each specific case. Moreover, for some applications (e.g., when employing this approach in a Monte-Carlo setup) this is not possible due to computational reasons because of the large memory size that the grid would end up having. Consequently, other methods that reduce this error calculation-wise have been developed.

For example, the *sub-harmonic method* (Sedmak, 1998) decreases the inaccuracies in the low-wavenumber region by replacing in the wavenumber domain the single sample at the origin by nine (or even more) sub-samples. These samples represent an equivalent length that is three times higher the length of a simple grid, allowing to sample the PSD at lower wavenumbers and enhancing the dataset accuracy at high spatial scales.

Another corrective method, proposed in Xiang (2014), implements a modal decomposition of the correlation function. The correlation function is pre-processed by extracting the piston and tilt components and a mask is applied. The tilt and piston components are then used to compute a tilt screen that is added to the dataset generated using Eq. (12). However, the drawback of such methods is that they are not of general nature (i.e., they cannot be applied for all kinds of PSDs), hence it is needed

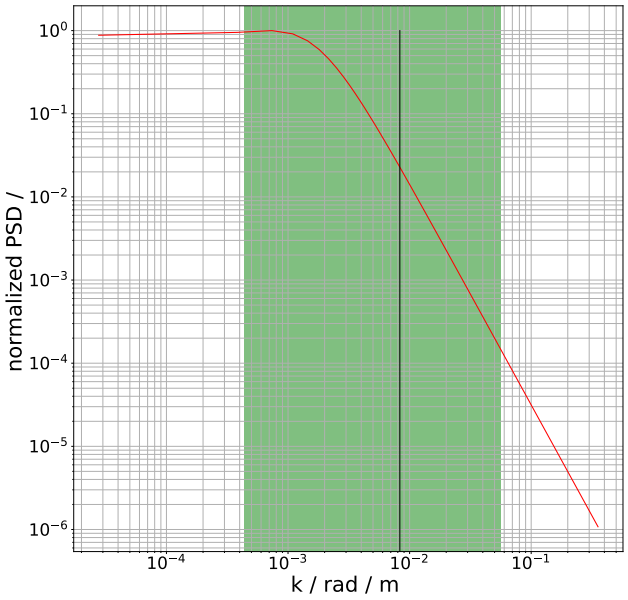

Figure 2. The spatial grid acting as band-pass filter. The green rectangle represents the considered wavenumbers for a spatial domain of the order of three times the outer scale, in this case it is expected to underestimate the power both at the high and the low wavenumbers. The red line represents the VK spectrum, and the black line represents the turbulence outer scale.

to compute different weighting parameters to the PSD from spatial domain to spatial domain. Moreover, these methods can be applied only on square grids.

5 The CB-RPM: generating the wind field from the correlation tensor

The here proposed CB-RPM has been developed with the aim of eliminating the bandpass effect of the DFT arising while using the RPM. To solve this problem, the relation between the correlation function and the PSD (i.e., the two quantities being a Fourier pair, as expressed in Eq. (8)) can be used. Indeed, by using the theoretical correlation function, computed on the spatial domain $\boldsymbol{s}$, to generate the PSD used in the dataset's synthesis, the sampling error is eliminated. This solution, and how to generate a stochastic dataset from it, has been first investigated theoretically in Cramer and Leadbetter (1967), from which several methods, mainly used in the field of geostatistics, have followed. Some of these methods (Dietrich and Newsam, 1993; Wood and Chan, 1994) rely on embedding a Toeplitz correlation matrix, computed from the correlation function, in a circulant matrix, synthesizing the desired dataset from its eigenvalue decomposition. However these methods do not allow to compute the dataset directly from the wind correlation function. Another proposed method, the FIM (Pardo-Iguzquiza and Chica-Olmo, 1993), is very similar to the here proposed CB-RPM, computing the PSD from the correlation function. However, no arrangements of the Fourier coefficients on the wavenumber domain before computing the dataset are needed in the latter one. The CB-RPM can be described by the following steps:

1. **Compute the correlation function**: in the case of a homogeneous turbulent wind field, the correlation tensor can be computed as (Batchelor, 1953):

$$B_{pq}(\boldsymbol{r}) = \sigma^2 \left[\frac{r_p r_q}{\boldsymbol{r}^2} f(\boldsymbol{r}) + \left(\delta_{pq} - \frac{r_p r_q}{\boldsymbol{r}^2} \right) g(\boldsymbol{r}) \right] ; \tag{16}$$

where δ_{pq} is the Dirac delta function, and $f(\boldsymbol{r})$ and $g(\boldsymbol{r})$ are the longitudinal and lateral correlation functions. In the case of a 2-D domain and assuming a VK spectrum, they are expressed by Eq. (14) and Eq. (15) respectively.

2. **Compute the PSD**: the corresponding PSD, $\Phi_{\text{CB-RPM}}(\boldsymbol{k})$, is the Fourier transform of the computed correlation function, $B_{pq}(\boldsymbol{r})$:

$$\Phi_{\text{CB-RPM}}(\boldsymbol{k}) = \mathcal{F}(B_{pq}(\boldsymbol{r})) ; \tag{17}$$

the obtained $\Phi_{\text{CB-RPM}}$ is not the theoretical PSD, but it is the discrete Fourier pair of the theoretical correlation function $B_{pq}(\boldsymbol{r})$ on the desired spatial domain. Note that $\Phi_{\text{CB-RPM}}(\boldsymbol{k})$ is not a tensor, as in Mann (1998), because it is the Fourier transform of the tensor component B_{pq}, and not of the whole tensor. This component takes already into account the longitudinal and lateral correlation, as expressed in Eq. (16).

3. **Synthesize the dataset**: the random dataset $u_p(\boldsymbol{s})$ can be generated by taking the real or imaginary component of the DIFT of the square root of the PSD $\Phi_{\text{CB-RPM}}(\boldsymbol{k})$, multiplied with a set of complex Gaussian random variables with zero mean and unity variance $\mu(\boldsymbol{k})$:

$$u_p(\boldsymbol{s}) = \text{Re/Im} \left\{ \mathcal{F}^{-1} \left(\mu(\boldsymbol{k}) \sqrt{\Phi_{\text{CB-RPM}}(\boldsymbol{k}) N} \right) \right\} . \tag{18}$$

The novelty of the CB-RPM w.r.t. the FIM lies in this last step. Indeed the CB-RPM does not need to divide the wavenumber domain in different regions where the amplitude spectrum's coefficients (i.e., the square root of the PSD) are computed, as it's needed in the FIM, but the PSD $\Phi_{\text{CB-RPM}}$ is directly used in the computation, resulting in a faster computation having one step less than the FIM.

6 Validating the CB-RPM at different spatial domains

As an example of the CB-RPM application, a single component wind field has been generated on a 2-D domain using the same parameters as in Section 4. In the case of a 2-D domain and considering the velocity along the x-axis, the generated wind field $u_x(\boldsymbol{s})$ is:

$$u_x(\boldsymbol{s}) = \text{Re/Im} \left\{ \mathcal{F}^{-1} \left(\mu(\boldsymbol{k}) \sqrt{\mathcal{F}\left(B_{xx}(\boldsymbol{r})\right) N_x N_y} \right) \right\} ; \tag{19}$$

where B_{xx} is the VK correlation function, computed using Eq. (13). The synthesized wind field u_x, its structure function, and the expected one are represented in Fig. (3). The expected structure function matches exactly the theoretical one, demonstrating that the synthesized dataset $u_x(\boldsymbol{s})$ respects the required statistics.

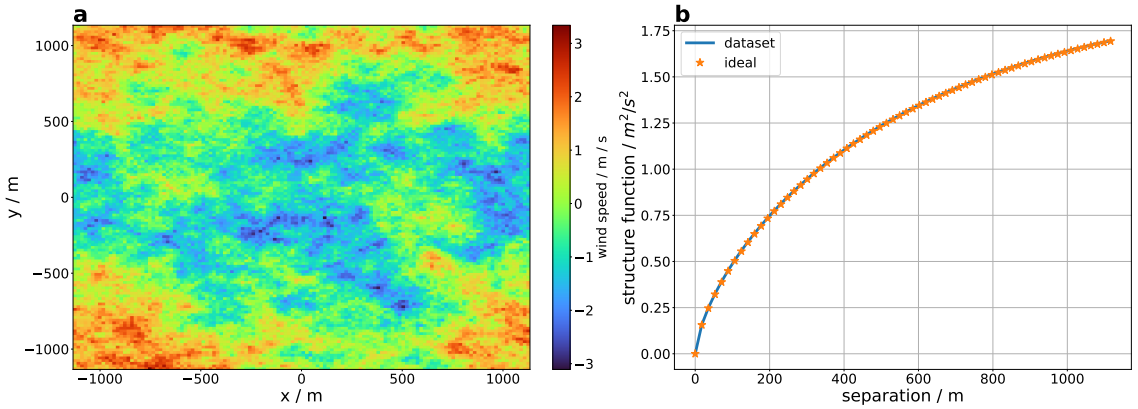

Figure 3. A 2-D wind field example generated by the CB-RPM. Fig3a: a single wind field generated using the CB-RPM. Fig3b: theoretical structure function in orange stars, dataset's expected structure function in blue.

In order to verify the actual generality of the method (i.e., it can be used without the need for any parameter optimization on any spatial domain), the expected structure function has been calculated for a wide range of spatial grid dimensions, starting from $0.01L_0$ up to $10L_0$. Similar to the function Φ_{FFT} in Xiang (2014), for very small spatial domains w.r.t. the turbulence outer scale L_0, the obtained PSD, $\Phi_{\text{CB-RPM}}(\boldsymbol{k})$, yields negative values. This is theoretically incorrect, because the PSD is defined as a positive function. The cause of the occurrence of these negative values is due to the implementation of the DFT on very small spatial domains. In fact, for very small spatial domains, the correlation function becomes almost flat, requiring some of the DFT coefficients to be phase-shifted by a factor π (i.e., having negative-amplitude values) in order to synthesize the desired shape in the spatial domain. Considering the extreme case in which the correlation function is a circular flat surface, its Fourier transform would be a *jinc* function (Goodman, 1996). So the appearance of negative values in $\Phi_{CB-RPM}(\boldsymbol{k})$ is expected for very small spatial domains. One simple solution would be to take the absolute value of $\Phi_{CB-RPM}(\boldsymbol{k})$, however this would lead to an error in the dataset's correlation function as shown in Fig. (4), where a single component wind field is generated on a 2-D, 8×8 grid, of length $0.1L_0$ and $L_0 = 756$ m.

To tackle the issue regarding negative PSD values, it is possible to consider only the positive part of the PSD, and reduce the error by pre-compensating the correlation function, as proposed in Xiang (2014). Considering the example presented in Fig. (3), where the theoretical correlation function has been used without any compensation, this pre-compensation consists in updating the correlation function used in the PSD computation by subtracting to the theoretical correlation function, defined in Eq. (13), the weighted error generated by neglecting the negative-amplitude wavenumbers of the PSD:

$$B_W(\boldsymbol{r}) = B_{xx}(\boldsymbol{r}) - W(\boldsymbol{r})\Delta_\Phi(\boldsymbol{r})\,; \tag{20}$$

where the error $\Delta_\Phi(\boldsymbol{r})$ is computed as:

$$\Delta_\Phi(\boldsymbol{r}) = B_{xx}(\boldsymbol{r}) - \mathcal{F}\left[H\left(\Phi_{\text{CB-RPM}}(\boldsymbol{k})\right)\Phi_{\text{CB-RPM}}(\boldsymbol{k})\right]\,; \tag{21}$$

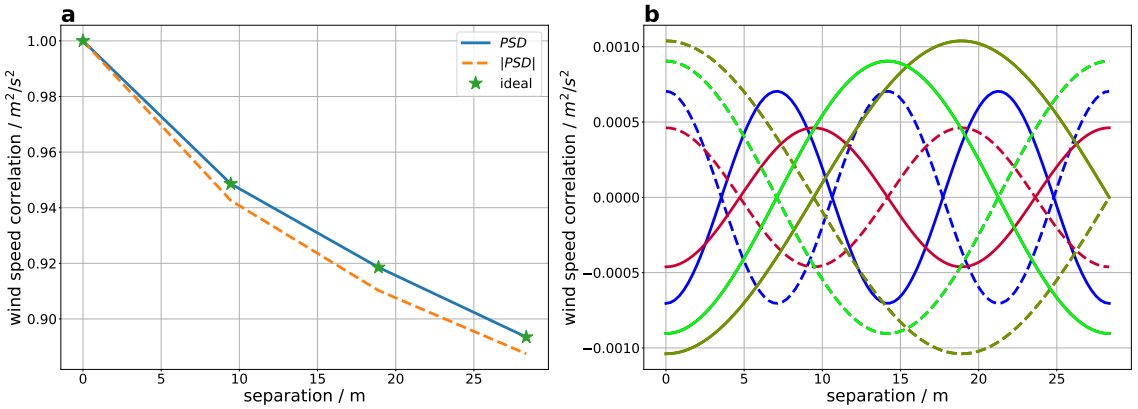

Figure 4. Negative DFT coefficients contribution. Fig4a: the theoretical correlation function in green stars, the correlation function computed assuming negative values in the PSD in blue, the correlation function computed using the absolute value of the PSD in dashed orange. Fig4b: the different colors represent the contribution to the correlation function computation of different DFT coefficients. The contribution of the negative coefficients is represented by continuous lines, the contribution of the same coefficients but with a positive value in dashed lines. The difference between the sum of the two sets of lines gives the expected error in using the absolute value of the PSD.

Table 1. Compensation parameters

A	$\frac{65}{\left(\frac{L}{L_0}-0.7\right)1.2\sqrt{2\pi}} e^{-\frac{\left[\log\left(\frac{L}{L_0}-0.7\right)-1.7\right]^2}{2\times 1.2^2}} - 6.4$
C	2
E	$L^2/530$
F	$L^2/530$
g	0.3

where $H()$ is the Heaviside function, and the weight $W(\boldsymbol{r})$ has the shape of an elliptic super Gaussian window:

$$W(\boldsymbol{r}) = A\mathrm{e}^{-C\left[\left(\frac{r_x}{E}\right)^g+\left(\frac{r_y}{F}\right)^g\right]}; \tag{22}$$

where g is the super Gaussian function exponent, and A, C, E, F are parameters that can be optimized depending on the PSD and the required dataset's accuracy. The parameters proposed for a square 64×64 grid, of dimension $L\times L$, and a VK spectrum are reported in Table 1. These parameters were found by optimizing the dataset error for different spatial domains. By using the weighted CB-RPM (WCB-RPM) with these parameters, the obtained error is three to five times lower than using the CB-RPM for very small spatial domains w.r.t. the turbulence outer scale L_0. In this case Eq. (19) becomes:

$$u_p(\boldsymbol{s}) = \mathrm{Re}\left\{\mathcal{F}^{-1}\left(\mu(\boldsymbol{k})\sqrt{\mathcal{F}\left(B_W(\boldsymbol{r})\right)N_xN_y}\right)\right\}. \tag{23}$$

7 Comparing the RPM and the CB-RPM

The errors of both methods have been compared on a wide range of spatial grid dimensions, starting from $0.01L_0$ up to $10L_0$. For each grid, the method error Δ_i has been computed as:

$$\Delta_i = \max(\varepsilon(\boldsymbol{r}_i)); \tag{24}$$

where $\varepsilon(\boldsymbol{r}_i)$ is computed using Eq. (10) for the separation vector $\boldsymbol{r}_i$, and the dataset's structure function $D(\boldsymbol{r}_i)$ is computed using Eq. (9), where the dataset's correlation function is computed as:

$$B(\boldsymbol{r}_i) = \overline{u_x(\boldsymbol{s})u_x(\boldsymbol{s}+\boldsymbol{r}_i)^*}. \tag{25}$$

It has been decided to consider the maximum error value for each spatial domain for conservative reasons. The comparison between the two methods is represented in Fig. (5), where it is clear how the CB-RPM outperformed the RPM of at least one order of magnitude, confirming that the method is a reliable solution in the synthesis of Gaussian processes without the need for any parameter optimization. For spatial domains greater than $2.5L_0$, a region which is relevant e.g. for the simulation of aircraft turbulence encounters (Kiehn et al., 2022), the CB-RPM can be declared as *exact in principle* (Wood and Chan, 1994), meaning that the method error is limited by the computer arithmetic inaccuracies. The novelty of the CB-RPM w.r.t. the RPM lies in its performance, especially for spatial domains greater than $2.5L_0$, as represented in Fig. (5). If a greater accuracy is needed at low spatial domains the WCB-RPM can be used by implementing Eq. (23) (dashed green line in Fig. (5)). The proposed solution reduces the error up to two orders of magnitudes w.r.t. the RPM. It should be noted that the WCB-RPM parameters presented here can be further optimized. However, this is left to possible later applications, as the authors' objective is to generate wind fields for spatial domains around $20L_0$, where the CB-RPM performs excellently. Initially it was thought to compare the synthesized datasets using their PSDs, but to avoid the biases generated by computing the dataset's PSD using Eq. (7), and the underestimation of the dataset's power due to windowing (Thomson, 1982), it was considered more appropriate to compare the synthesized datasets' correlation functions, computed using Eq. (25). For the Wiener–Khinchin theorem, the datasets' correlation functions are the Fourier transform of the PSDs. Thus, in the case the errors of the datasets' correlation functions w.r.t. the theoretical ones are low, this applies also to the errors of the datasets' PSDs.

8 Conclusions

In this publication a new generating method for synthesizing Gaussian and stationary phenomena has been presented. This new method allows the generation of a dataset with an error of at least one order of magnitude lower than the commonly used RPM. For spatial domains greater than $2.5L_0$, the CB-RPM can be declared as exact in principle. This refers to the computational errors, not to how close the synthesized wind field is to reality. Indeed, the reason in developing the CB-RPM has been to decrease the errors of the synthesized wind field w.r.t the theoretical structure function, not real data. In this paper the assumption of homogeneous and isotropic turbulence has been made. However, especially for turbulence near the surface, this assumption is no longer valid (Panofsky and Dutton, 1984). In this case, the wind field correlation function can

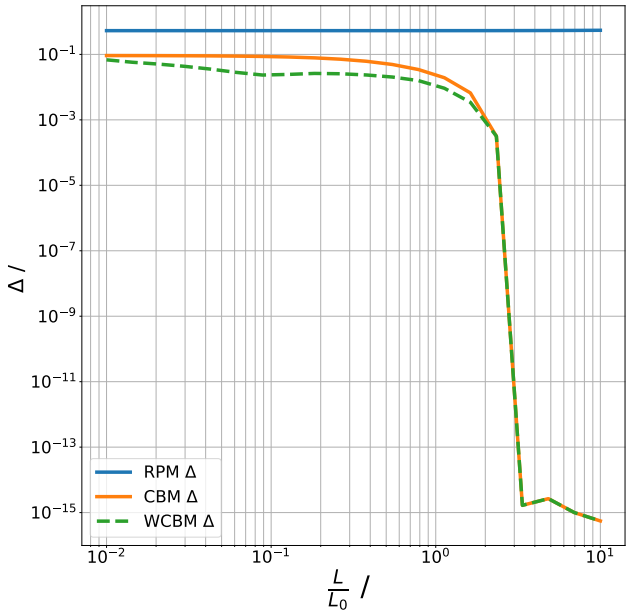

Figure 5. Methods comparison. RPM error in blue, CB-RPM error in orange, WCB-RPM in dashed green. The x axis indicates the ratio between the considered spatial domain and the turbulence outer scale.

be refined by computing it from real data, measured using anemometers or five-hole probes, from high resolution Large Eddy Simulation (LES) results (Yoshimura et al., 2023), or by considering a non-stationary wind and using the method presented in (Wilson, 1997). The authors are working to expand the use of CB-RPM to these cases as well. Furthermore, being a general method, it can be used to synthesize any phenomenon considered Gaussian and stationary (e.g., index of refraction fluctuations, temperature fluctuations, homogeneous and isotropic turbulence) only by knowing the phenomenon's structure or correlation function. These can be obtained through analytical solutions (e.g., from the Kolmogorov cascade theory (Kolmogorov, 1941)) or from real measurement data, allowing to synthesize phenomena for which no analytical solutions exist (e.g., Clear Air Turbulence (CAT) events (Knox, 1997)). A further advantage of the method is that it allows, in a relatively simple way, the representation of anisotropies in the phenomenon of interest: these can be directly added to the theoretical correlation from which the PSD is computed (Pardo-Iguzquiza and Chica-Olmo, 1993). The method is valid also for non-symmetrical spatial domains, an interesting result that can be applied to highly customized wind speed dataset generation. The authors are working on adding other types of spectra (e.g., the Kaimal spectrum (Kaimal et al., 1972) or the Mann uniform shear turbulence model (Mann, 1994)) to the CB-RPM. A further development would be the use of the CB-RPM for the synthesis of wind fields starting from any wind dataset provided by the user. This would allow to further investigate anisotropies found during aircraft measurements (Nowak et al., 2025), but still assuming homogeneous turbulence. Moreover, it is foreseen to implement the possibility of adding non-Gaussian features to the synthesized wind field, following the method proposed in (Friedrich et al., 2022), or to generate non-stationary wind fields. Finally, a routine to automatically compute the weighting function $W(\boldsymbol{r})$

starting from the error $\Delta_\Phi(\boldsymbol{r})$ is being developed. This would allow to achieve better performance on small spatial domains w.r.t. the turbulence outer scale L_0.

Author contributions. Problem statement: PV; conceptualization: all authors; methodology: MF; software: MF and DK; verification: DK; writing—review and editing: all authors. All authors have read and agreed to the published version of the manuscript.

Competing interests. The authors declared that there are no competing interests.

Disclaimer. Co-Funded by the European Union. Views and opinions expressed are however those of the authors only and do not necessarily reflect those of the European Union or Clean Aviation Joint Undertaking. Neither the European Union nor the granting authority can be held responsible for them.

Acknowledgements. This study was performed within the framework of the UP Wing project. The project Ultra Performance Wing (UP Wing, project number: 101101974) is supported by the Clean Aviation Joint Undertaking and its members. The authors would like to acknowledge Dr. Tobias Bölle (DLR), Lukas Bührend (DLR), and Prof. Dr. Christoph Kiemle (DLR) for the insightful comments and fruitful discussion. Moreover, the suggestions of one anonymous reviewer greatly increased the quality of the publication. Many thanks for your time.

References

Andrews, L. C. and Phillips, R. L.: Laser Beam Propagation in Random Media, SPIE Press, Bellingham, Washington, USA, ISBN 978-08-19478-32-0, https://doi.org/https://doi.org/10.1117/3.626196, 2005.

Baran, A. J. and Infield, D. G.: Simulating atmospheric turbulence by synthetic realization of time series in relation to power spectra, Journal of Sound and Vibration, 180, 627–635, https://doi.org/10.1006/jsvi.1995.0103, 1995.

Batchelor, G. K.: The Theory of Homogeneous Turbulence, Cambridge University Press, 1953.

Beghi, A., Cenedese, A. C., and Masiero, A.: Multiscale stochastic approach for phase screen synthesis, Applied Optics, 50, 4124–4133, https://doi.org/10.1364/AO.50.004124, 2011.

Borgman, L., Taheri, M., and Hagan, R.: Three-Dimensional, Frequency-Domain Simulations of Geological Variables, In: Geostatistics for Natural Resources Characterization., https://doi.org/10.1007/978-94-009-3699-7_30, 1984.

Chen, Y., Guo, F., Schlipf, D., and Cheng, P. W.: Four-dimensional wind field generation for the aeroelastic simulation of wind turbines with lidars, Wind Energy Science, 7, 539 – 558, https://doi.org/10.5194/wes-7-539-2022, 2022.

Cholesky, A. L.: Sur la résolution numérique des systèmes d'équations linéaires, Bulletin de la Sabix, https://doi.org/10.4000/sabix.529, 1910.

Cooley, J. W. and Tukey, J. W.: An Algorithm for the Machine Calculation of Complex Fourier Series, Mathematics of Computation, 1965.

Cramer, H. and Leadbetter, M. R.: Stationary and Related Stochastic Processes, John Wiley & Sons, Inc., 1967.

CS25: Certification Specifications for Large Aeroplanes, Regulation, EASA, 2023.

Dietrich, C. R. and Newsam, G. N.: A fast and exact method for multidimensional Gaussian stochastic simulations, Water Resources Research, 29, https://doi.org/10.1029/93WR01070, 1993.

Fried, D. L.: Statistics of a Geometric Representation of Wavefront Distortion, Journal of the Optical Society of America, 55, https://doi.org/10.1364/JOSA.55.001427, 1965.

Friedrich, J., Moreno, D., Sinhuber, M., Wächter, M., and Peinke, J.: Superstatistical Wind Fields from Pointwise Atmospheric Turbulence Measurements, PRX Energy I, https://doi.org/10.1103/PRXEnergy.1.023006, 2022.

Goodman, J. W.: Introduction to Fourier Optics, McGraw-Hill, 1996.

Hoblit, F. M.: Gust Loads on Aircraft: Concepts and Applications, AIAA Education Series, Washington, D.C., ISBN 978-0-930403-45-4, https://doi.org/10.2514/4.861888, 1988.

IEC61400-1: Wind energy generation systems - Part 1: Design requirements, Standard, IEC, 2019.

Johansson, E. M. and Gavel, D. T.: Simulation of stellar speckle imaging, in: Amplitude and Intensity Spatial Interferometry II, edited by Breckinridge, J. B., vol. 2200, pp. 372–383, SPIE, https://doi.org/10.1117/12.177254, 1994.

Kaimal, J. C., Wyngaard, J. C., Izumi, Y., and Coté, O. R.: Spectral characteristics of surface-layer turbulence, Quarterly Journal of the Royal Meteorological Society, 98, https://doi.org/10.1002/QJ.49709841707, 1972.

Kiehn, D., Fezans, N., Vrancken, P., and Deiler, C.: Parameter Analysis of a Doppler Lidar Sensor for Gust Detection and Load Alleviation, in: International Forum on Aeroelasticity and Structural Dynamics (IFASD), 13–17 June 2022, Madrid, Spain, pp. 1385–1404, ISBN 9781713871125, https://doi.org/10.60801/IFASD-2022-105, 2022.

Knox, J. A.: Possible Mechanisms of Clear-Air Turbulence in Strongly Anticyclonic Flows, Monthly Weather Review, 125, https://doi.org/10.1175/1520-0493(1997)125<1251:PMOCAT>2.0.CO;2, 1997.

Kolmogorov, A. N.: The local structure of turbulence in incompressible viscous fluid for very large Reynolds numbers, Doklady Akademii Nauk SSSR, 30, 1941.

Lane, R. G., Glindemann, A., and Dainty, J. C.: Simulation of a Kolmogorov phase screen, Waves in Random Media, 2, 209, https://doi.org/10.1088/0959-7174/2/3/003, 1992.

Mann, J.: The spatial structure of neutral atmospheric surface-layer turbulence, J. Fluid Mech., 273, https://doi.org/10.1017/S0022112094001886, 1994.

Mann, J.: Wind field simulation, Probabilistic Engineering Mechanics, 13, 269–282, https://doi.org/10.1016/S0266-8920(97)00036-2, 1998.

Nowak, J. L., Lothon, M., Lenschow, D. H., and Malinowsi, S. P.: The ratio of transverse to longitudinal turbulent velocity statisticsfor aircraft measurements, AMT, 18, https://doi.org/10.5194/amt-18-93-2025, 2025.

Panofsky, H. A. and Dutton, J. A.: Atmospheric Turbulence, John Wiley & Sons, Inc., 1984.

Pardo-Iguzquiza, E. and Chica-Olmo, M.: The Fourier Integral Method: An efficient spectral method for simulation of random fields, Mathematical Geology, 25, 177–217, https://doi.org/10.1007/BF00893272, 1993.

Sedmak, G.: Performance analysis of and compensation for aspect-ratio effects of fast-Fourier-transform-based simulations of large atmospheric wave fronts, Applied Optics, 37, 4605–4613, https://doi.org/10.1364/AO.37.004605, 1998.

Shannon, C. E.: Communication in the Presence of Noise, Proceedings of the IRE, 1949.

Shinozuka, M. and Jan, C. M.: Digital simulation of random processes and its applications, Journal of Sound and Vibration, 25, 111–128, https://doi.org/10.1016/0022-460X(72)90600-1, 1972.

Tatarski, V. I.: Wave propagation in a turbulent medium, McGraw-Hill Book Company, Inc., 1961.

Thomson, D. J.: Spectrum estimation and harmonic analysis, Proceedings of the IEEE, 70, https://doi.org/10.1109/PROC.1982.12433, 1982.

Wiener, N.: Generalized Harmonic Analysis, Acta Math., https://doi.org/10.1007/BF02546511, 1930.

Wilson, D. K.: Three-Dimensional Correlation and Spectral Functions for Turbulent Velocities in Homogeneous and Surface-Blocked Boundary Layers, Army Research Laboratory: Adelphi, MD, USA, 1997.

Wilson, D. K.: Turbulence Models and the Synthesis of Random Fields for Acoustic Wave Propagation Calculations, Army Research Laboratory: Adelphi, MD, USA, 1998.

Wold, J. W., Stadtmann, F., Rasheed, A., Tabib, M., San, O., and Horn, J.-T.: Enhancing wind field resolution in complex terrain through a knowledge-driven machine learning approach, Engineering Applications of Artificial Intelligence, https://doi.org/10.1016/j.engappai.2024.109167, 2024.

Wood, A. T. A. and Chan, G.: Simulation of Stationary Gaussian Processes in [0, 1], Journal of Computational and Graphical Statistics., 3, https://doi.org/10.2307/1390903, 1994.

Xiang, J.: Fast and accurate simulation of the turbulent phase screen using fast Fourier transform, Optical Engineering, 53, https://doi.org/10.1117/1.OE.53.1.016110, 2014.

Yoshimura, R., Ito, J., Schittenhelm, P. A., Suzuki, K., Yakeno, A., and Obayashi, S.: Clear Air Turbulence Resolved by Numerical Weather Prediction Model Validated by Onboard and Virtual Flight Data, Geophysical Research Letters, https://doi.org/10.1029/2022GL101286, 2023.